ABBD: accumulated band-wise binary distancing for unsupervised parameter-free hyperspectral change detection.

LI, Y., REN, J., YAN, Y., MA, P., ASSAAD, M. and GAO, Z.

2024

ABBD: Accumulated Band-Wise Binary Distancing for Unsupervised Parameter-Free Hyperspectral Change Detection

Yinhe Li, Jinchang Ren, *Senior Member, IEEE*, Yijun Yan, *Member, IEEE*, Ping Ma, Maher Assaad, and Zhi Gao, *Member, IEEE*

***Abstract*—As a fundamental task in remote sensing earth observation, hyperspectral change detection (HCD) aims to identify the changed pixels in bitemporal hyperspectral images. However, the water-absorption effect, poor weather conditions, noise and inconsistent illumination as well as lack of accurate ground truth has made HCD particularly challenging. To tackle these challenges, a novel Accumulated Band-wise Binary Distancing (ABBD) model was proposed for unsupervised parameter-free HCD. Rather than relying on the absolute pixel difference with thresholding in conventional approaches, the binary distancing only indicated whether a pixel was changed or not in a certain band, which could alleviate the adverse effects of noise-induced inconsistency of measurement. The band-wise binary distance map is then accumulated to form a grayscale change map, on which the simple *k*-means was applied for a final binary decision-making. Experiments on three publicly available datasets have validated the superiority of our approach, which has yielded comparable or slightly better results in comparison to a few state-of-the-art methods including several deep learning models.**

***Index Terms*—Accumulated band-wise binary distancing (ABBD), hyperspectral image (HSI), parameter-free, unsupervised change detection.**

I. Introduction

BY COMBINING the pixel-wise 1-D spectral data and the integrated spectroscopy as a standard 2-D image, hyperspectral images (HSI) can reveal a wealth of information for characterizing the physical and chemical properties of the objects [1]. In comparison to multispectral images and color images in Red-Green-Blue (RGB), HSI has two distinct advantages. The first is its high spectral resolution and a wide spectral range that encompasses the visible, near-infrared, and even short-wave infrared and ultraviolet ranges, enabling monitoring and inspection well beyond human vision. HSI can capture detailed spectral information with a resolution at 10 nm or less, consisting of hundreds of continuous spectral bands [2]. The second is the rich spatial and spectral information contained in HSI, making it highly effective in a wide range of detection, inspection, classification and quality grading tasks [3], including change detection and land mapping in remote sensing earth observation [4].

As a subtask of pattern recognition, change detection is often used to identify and quantify variations between images of the same scene at different times or under different imaging conditions [5]. With the rapidly increased availability of the HSI, HCD has received significant attention, especially for detecting small but important changes that appear to be spatially and/or spectrally distinct in between. This is particularly useful in geological surveys [6], disaster monitoring [7], urban planning [8], and agricultural surveys [9].

Despite the rich spatial and spectral information, HSI often suffers from highly redundant content and various aspects of noise, due mainly to the sensor limitations and atmospheric effects during the data acquisition. In the last decades, many HCD methods have been explored to tackle these issues, including unsupervised and supervised ones, as detailed below.

For unsupervised HCD, image algebra-based classic approaches are popularly used, in which pixel-wise difference is measured against a threshold to determine the changed pixels These include the change vector analysis (CVA) [10] and spectral angle mapper (SAM) [11]. CVA detects the changes by calculating the Euclidean distance between the bitemporal pixels in the spectral domain, whilst SAM uses the angle between the two spectral vectors to determine their similarity. The dynamic time warping (DTW) [12] was utilized to measure the spectral similarity by computing the minimum cumulative distance of corresponding pixels across all bands. Due to the atmospheric effects, sensor noise and other factors, the same object may show large variations, yet different objects may share similar spectrums. Therefore, these HCD methods tend to perform relatively poorly, as they rely simply on the pixel-based difference.

Manuscript received 22 January 2024; revised 6 March 2024 and 17 April 2024; accepted 21 May 2024. Date of publication 30 May 2024; date of current version 11 June 2024. This work was supported in part by Ajman University under Grant 2022-IRG-ENIT-2 for M. Assaad, and in part by the Guangdong Provincial Department of Education "Innovation and Strengthening University" under Grant 2022ZDJS015 for GPNU (Guangdong Polytechnic Normal University), Guangzhou, China. *(Corresponding author: Jinchang Ren.)*

Yinhe Li, Jinchang Ren, and Ping Ma are with the National Subsea Centre, Robert Gordon University, AB21 0BH Aberdeen, U.K. (e-mail: jinchang.ren@ieee.org).

Yijun Yan is with the School of Science and Engineering, University of Dundee, DD1 4HN Dundee, U.K.

Maher Assaad is with the Department of Electrical and Computer Engineering, Ajman University, Ajman 346, UAE.

Zhi Gao is with the School of Remote Sensing and Information Engineering, Wuhan University, Wuhan 430079, China.

Digital Object Identifier 10.1109/JSTARS.2024.3407212

Rather than using the raw spectral data, image transformation-based methods calculate the pixel difference in the transformed (feature) domain in order to highlight the changed features whilst reducing the dimension and redundancy of the data. One typical method is the principal component analysis (PCA) [13], which projects linearly the high-dimensional HSI data to a low-dimensional space whilst preserving most of the energy or information, though PCA is noise sensitive and computational expensive. In multivariate alteration detection (MAD) [14], changed pixels were extracted by applying the canonical correlation analysis to increase the variance of independently transformed variables. In [15], iteratively reweighted (IR) MAD was proposed by iterating the weights of different observations, where larger weights were assigned to observations with fewer changes, and vice versa. Although image transformation-based methods may perform well in occasions, they suffer from poor explain ability, due to failed preservation of the band-wise correlations and spectral characteristics of the HSI and are often computationally expensive.

Recently there are also other unsupervised HCD methods proposed. In [16], a novel three-order Tucker decomposition and reconstruction detector was proposed, which combines a singular value accumulation to determine the principal components in the factor matrices, Tucker decomposition and reconstruction to eliminate the influence of various factors in the multitemporal dataset, and SAM to analyze spectral changes after tensor processing in different domains. In [17], multitemporal HCD was proposed, based on discrete representation of change information, focusing on the represented change information in each spectral band. The band-wise radiation information is analyzed to generate a quantized discrete representation of the change vector, followed by a tree representation to distinguish between different types of changes. In [18], an automated image analysis method was proposed that relies on the utilization of difference images and histogram statistics for change detection. This method distinguishes alterations based on both positive and negative values within the difference image and establishes location-specific thresholds by identifying minimum points within the histogram. Despite reported success, most of these methods rely on certain manual intervention, incorporating excessive number of parameters, and lack of generality. In [19], a spatial-contextual feature extraction method was proposed that incorporated band selection to reduce spectral redundancy and an iterative spatial-adaptive filter for noise reduction. The change magnitude was evaluated using CVA and adaptive regions, followed by a binary thresholding using the Otsu method.

In recent years, a few unsupervised deep learning networks that do not rely on reference change maps have been proposed. In [20], an unsupervised context-sensitive framework based on deep CVA and suboptimal pretrained multilayered CNN was proposed, where the extracted deep features enabled to model the spatial relationships among neighboring pixels and complex objects. In [21], an untrained framework with randomly initialization and spatial-channel augmentation was proposed, which used successive dilation-deformable feature extraction blocks to extract multiscale spatial-spectral features and a change-sensitive feature augmentation and comparison module for feature fusion. In [22], an unsupervised framework based on regular convolutions with fixed kernels as feature extractors was proposed that extracted bitemporal features using an untrained model and utilized deep change vector analysis to distinguish changed pixels from unchanged ones. Although it can help to reduce the dependence on labels, the detection accuracy is less desirable. In [23], a progressive pseudolabel framework was proposed that utilized the BCNN as the backbone and a multiscale preclassification module to generate initial pseudolabels. Subsequently, these pseudolabels were selected based on the uncertainty estimated by a Bayesian network. Although unsupervised deep learning-based methods relying on pseudolabels have the potential to eliminate the dependence on the ground truth, the detection accuracy is entirely reliant on the precision of the generated pseudolabels [24]. Supervised HCD methods include conventional machine learning and DL-based methods that train the networks using the labeled information from the ground truth map. In [25], pseudotraining data was generated using the Expectation Maximization strategy, along with an optimized random forest for determining a binary change map. In [26], band selection was applied first for dimension reduction, followed by the sequential spectral change vector analysis for feature extraction and the Support Vector Machine and random forest to determine the binary change maps. As a recent trend, deep learning (DL) has attracted significant attention in HCD to extract highly efficient and representative features in the spectral, spatial, and spectral-spatial domains of the HSI. In [27], a recurrent convolutional neural network (CNN) was proposed for HCD to extract the spectral-spatial-temporal features jointly, by combining the merits of the CNN and recurrent neural networks. In [28], an end-to-end 2-D CNN framework was proposed, using a mixed affinity matrix with an integrated subpixel representation for feature learning. In [29], a pixel-level self-supervised hyperspectral spatial-spectral feature understanding network was proposed for pixel-wise feature representation instead of 2-D band-based processing, where a powerful spatial-spectral attention module based on fully convolutional layers was employed to explore the spatial correlation and discriminative spectral features. In [30], a three-directions spectral-spatial CNN was proposed, which decomposes the change tensor into spectral and two spatial components. Spectral information is extracted and dimensionally reduced via 1-D convolution, while spectral-spatial features from the two spatial directions are obtained using 2-D convolution, encompassing information from diverse directions. In [31], a multiscale diff-changed feature fusion network was proposed that combined a reduced inception module and a cross-layer attention module to highlight the significant features at each scale. Furthermore, LSTM was employed to mine the temporal correlation between multitemporal images. In [32], a novel hierarchical attention feature fusion network was proposed, leveraging multiscale convolution fusion filters for exploring global semantic features. This network integrated a position attention module, and multiperspectives feature filter block with diverse kernel sizes, alongside a combined loss function to balance feature impacts during the backpropagation. In [33], a dual-branch transformer autoencoder was designed, with shared weights in the middle

layer of the dual-branch transformer, pulling features from different data into the same space. Moreover, the transformer autoencoder was also trained iteratively to align the domains. In [34], an advanced DL-based approach was introduced, employing an eigenvalue extrema-based band selection strategy to capture prominent attribute patterns in HSI, where pixel pair attributes were represented in bitemporal HSIs using a 3-D tensor with spectral-spatial sequence characteristics. It integrates a fusion framework of CNN and transformer encoder to extract high-order sequence semantic features, incorporating local context information and global sequence dependencies through a spatial-spectral attention mechanism. In [35], the fusion network integrated global and local features from multisource RS data, where CNNs and transformer were utilized for extracting the high frequency and low frequency features, respectively. In [36], a lightweight frequency-spectrum unfolding network was presented for spectral super-resolution of RGB video data. A CNN-based frequency-domain subnetwork was used to solve the data subproblem, recovering spatial detail information from the HSI, using a Transformer-based spectrum-domain subnetwork to address the prior subproblem, for reconstructing the spectral information of the HSI. Although supervised DL-based HCD methods can achieve good performance as reported, they often rely heavily on large training data and suffer from extremely high computational costs. As a result, develop unsupervised HCD remains of great importance [37].

To tackle the identified challenges above, we proposed an effective and robust yet computationally efficient method for unsupervised parameter-free HCD. The major contributions are summarized as follows.

1) We propose Accumulated Band-wise Binary Distancing (ABBD), a novel unsupervised method for HCD. By leveraging binary distancing to indicate if there is a band-wise change between corresponding pixels, ABBD can effectively mitigate the adverse effects of noise-induced measurement inconsistency.
2) To adaptively determine the tolerance level when reaching the binary distancing, a parameter-free solution is derived in ABBD for robustness and ease of deployment whilst maintaining a high accuracy.
3) By applying the *k*-means to the accumulated *N* grayscale change map, the conventional thresholding is avoided for robustness in binary decision-making. Experiments on three publicly available datasets have validated its superior efficacy and efficiency when compared to several state-of-the-art unsupervised and even deep learning-based methods.

II. Proposed Methodology

A Conventional Pixel Differencing

In bitemporal HCD tasks, let $T^{(1),(2)} \in \Re^{W*H*B}$ represent two HSIs captured at different times after spatial registration and spectral correction, where W, H, and B denote the numbers of rows, columns, and spectral bands, respectively. Let $T^{(1)}_{(i,j)} = [x_1,\ x_2, \ldots, x_B]$ and $T^{(2)}_{(i,j)} = [y_1,\ y_2, \ldots, y_B]$ denote a pair of spectral vectors at (i,j) in $T^{(1)}$ and $T^{(2)}$ ($i \in [1, W]$, $j \in [1,\ H]$), where x_b and y_b ($b \in [1, B]$) represent the corresponding intensity values at band b. The pixel-based band-wise distance between $T^{(1)}$ and $T^{(2)}$ can be calculated by

$$T^{\text{diff}}_{(i,j)} = \left|T^{(2)}_{(i,j)} - T^{(1)}_{(i,j)}\right| = [d_1, d_2,\ \ldots,\ d_B]\ ,$$
$$d^{(b)}_{(i,j)} = |y_b - x_b|\ ,\ b \in [1, B] \tag{1}$$

where $d^{(b)}_{(i,j)}$ is the difference of the corresponding pixel (i,j) at band b on two spectral vectors $T^{(1)}_{(i,j)}$ and $T^{(2)}_{(i,j)}$.

In unsupervised wisdom, changed pixels can be determined based on the magnitude of $T^{diff}_{(i,j)}$, the accumulated $d^{(b)}_{(i,j)}$ or the vector distance between $T^{(1)}_{(i,j)}$ and $T^{(2)}_{(i,j)}$ [38]. However, due to the inconsistent illumination [39], varying environmental and weather conditions and noise [40], $d^{(b)}_{(i,j)}$ often appears noise-sensitive, leading to quite unreliable results of HCD. In particular, the noise caused significant changes in certain bands may affect the overall decision-making even though the changes are minor in the majority of the bands. Therefore, more effective spectral matching is needed for more robust change detection in HSI.

To tackle the aforementioned issues, we propose to consider the band-wise matching in HCD and define $M_{(i,j)} \in \Re^{1*B}$ to indicate whether the pixel pair at (i,j) are changed or not. Four strategies are further proposed for improving the robustness of HCD as follows. The flowchart of the proposed ABBD algorithm is shown in Fig. 1.

B. Band-wise Binary Distancing

First, we apply a tolerance threshold ε to $d^{(b)}_{(i,j)}$, and the pair of pixels will be considered as changed at band b only if we have $d^{(b)}_{(i,j)} \geq \varepsilon$. This can help to determine a band-wise binary change map M as follows:

$$M^{(b)}_{(i,j)} = \begin{cases} 1 & \text{if } d^{(b)}_{(i,j)} \geq \varepsilon \\ 0 & \text{Otherwise.} \end{cases} \tag{2}$$

The strategy here has two advantages. First, the tolerance applied can filter the insignificant difference that is widely occurred in natural HSI scenes. More importantly, binary distancing can help to suppress the effect of noise caused by big changes in certain bands for more robust decision-making for robustness. By adopting band-wise binary distancing, the effect of abnormal values caused by noise can be mitigated in comparison to the absolute differences used in conventional approaches. This has been further validated in the experiment section.

C. Determining the Overall Change Map

Based on $M^{(b)}$, as our second strategy, the overall change for each pixel pair in $T^{(1)}$ and $T^{(2)}$ is decided by accumulating the band-wise binary change map by

$$C_{(i,j)} = \sum_{b=1}^{B} M^{(b)}_{(i,j)}\ ,\ C_{(i,j)} \in [0, B] \tag{3}$$

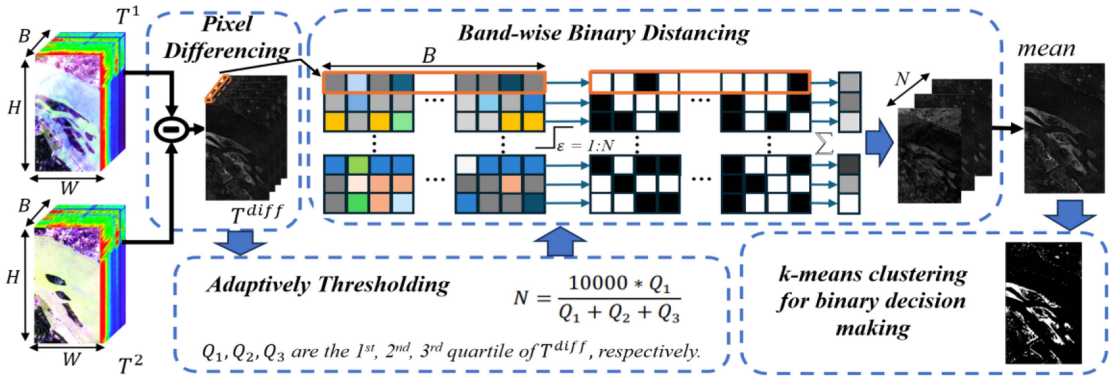

Fig. 1. Architecture of the proposed ABBD algorithm.

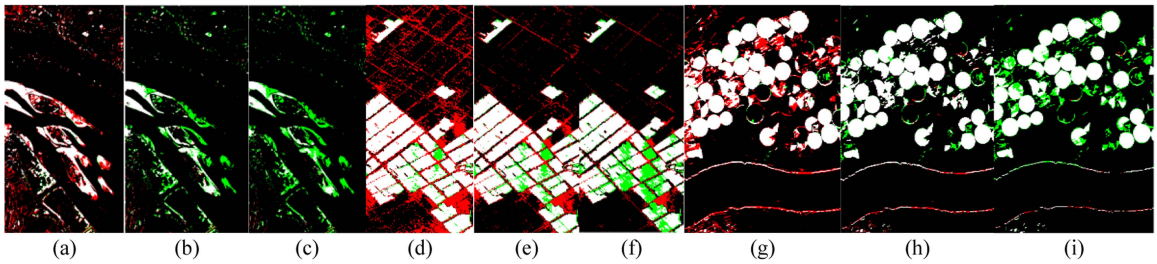

Fig. 2. Intermediate results of three datasets with ε equals to 300, 600, 900 on (a)–(c) River dataset; (d)–(e) Yancheng dataset; (g)–(i) Hermiston dataset, where false alarms and missing pixels are marked in red and green, respectively.

where C is a grayscale image to indicate the overall degree of changes in all the bands. Note the intensity of C is within [0, B], where B is the number of bands.

As the $M^{(b)}$ is a binary indicator to show whether there is a *noticeable* change at the corresponding pixel pairs, against a predetermined threshold ε, the extracted overall change map C is also sensitive to ε. For the three original datasets, the extracted change maps under different values of ε are shown in Fig. 2, where the values of ε are set to 300, 600, and 900, respectively.

As seen in Fig. 2, the change maps C are very sensitive to ε. Setting the fixed threshold too low can result in a higher number of false alarms as it incorrectly classifies pixels with subtle difference as changed ones. With an increasing ε, more false alarm pixels are suppressed, yet real changed pixel may also be filtered off if the corresponding difference is not high enough, leading to more missing pixels in the resulting binary image.

D. Adaptively Thresholding in Binary Distancing for Parameter-free Implementation

Due to the inherent challenge of determining the optimal ε for each dataset, we propose as the third strategy an iterative process to retrieve the best change map as follows. Herein, we automatically determine a new parameter N to bypass the fixed ε as follows:

$$N = \frac{V * Q_1}{Q_1 + Q_2 + Q_3} \tag{4}$$

where V is the coefficient used to ensure that the threshold aligns with the original data, which is set to 10 000 in this experiment as it helps to produce the best results. $Q_1, Q_2,$ and Q_3 are the first, second, and third quartile of T^{diff}, respectively.

Note the statistics here will reflect the distribution characteristics of pixel-wise difference in all spectral bands that statistical analysis based adaptive thresholding is employed for optimal decision-making, which helps to achieve a parameter-free implementation rather than relying on certain unadjusted parameters.

Subsequently, the final change map C_{acc} can be determined as the mean of the accumulated band-wise binary distancing results below, where $C^{(n)}$ denotes the change map with the parameter ε set to $n, n \in [1, N]$.

$$C_{\text{acc}} = \frac{1}{N} \sum_{n=1}^{N} C^{(n)}. \tag{5}$$

The extracted final grayscale change maps of three datasets are shown in Fig. 3, where the changed pixels are clearly distinguishable when comparing to the GT maps. This has verified the value of the third strategy for bypassing the threshold ε and reach a parameter-free solution. In addition, the consistent results in Fig. 3 have validated the efficacy of the introduced strategy.

E. Applying K-Means for Binary Decision-making

Rather than to apply the thresholding to the refined change map C_{acc}, the fourth strategy is to apply the *k*-means clustering method [41] to determine the final binary change map (Ω) for

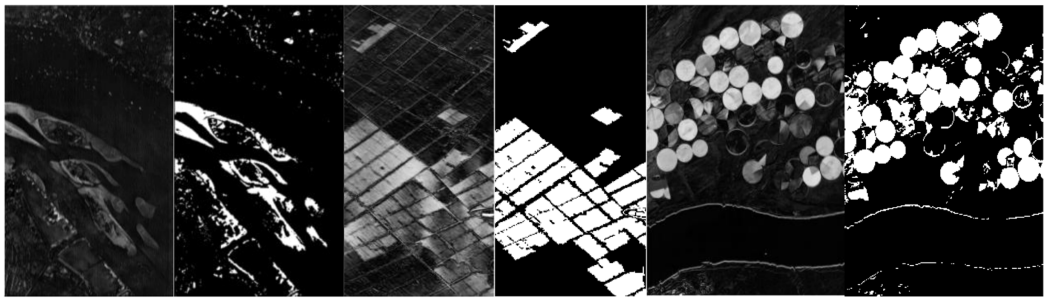

Fig. 3. Extracted change maps for the (a) River; (c) Yancheng; and (e) Hermiston datasets in comparison to the GTs in (b), (d), and (f).

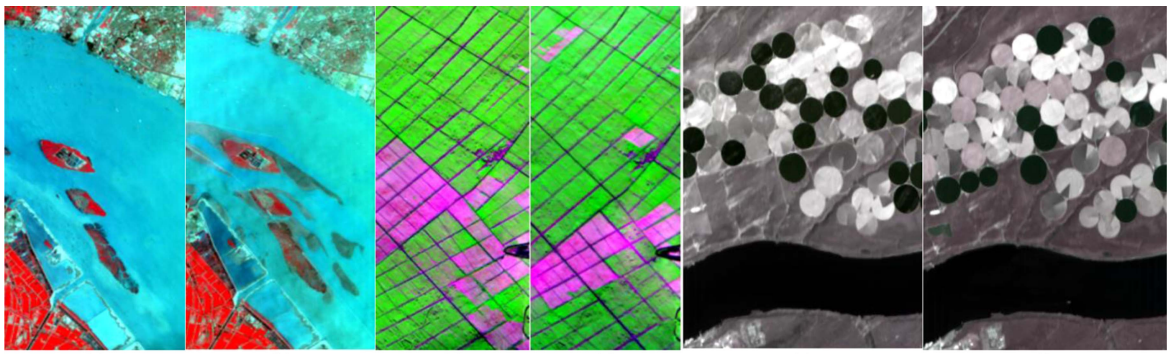

Fig. 4. Pseudocolored images of the three HSI datasets, including the River dataset captured on (a) May 3, 2013 and (b) Dec. 31, 2013, the Yancheng dataset captured on (c) May 3, 2006 and (d) April 23, 2007, and the Hermiston dataset captured on (e) May 1, 2004 and (f) May 8, 2007, respectively.

robustness as follows.

$$\Omega = kmeans\left(C_{\text{acc}}, k\right) \tag{6}$$

where $k = 2$ for binary classification to classify the change map C_{acc} into the changed foreground and the unchanged background accordingly before evaluation.

III. Experiments and Results

A. Dataset Description

All three datasets used in our experiment were acquired by the Hyperion sensor mounted onboard the Earth Observing-1 (EO-1) satellite, which offers up to 242 spectral bands ranging from 0.4–2.5 μm, with a spatial resolution of 10 m and a spectral resolution of 30 nm [42]. All the images are spatially aligned in pairs along with the noise removal, as seen in Fig. 4.

As shown in Fig. 4(a) and (b), the River dataset contains 463 $\times$ 241 spatial pixels and 198 spectral bands, where the major changes are the substance in the river and the structure of the riverbank. The Yancheng dataset shown in Fig. 4(c) and (d) has 420 $\times$ 140 spatial pixels and 154 spectral bands after noise removal, where the major change is the land cover on the wetlands. For the Hermiston dataset given in Fig. 4(e) and (f), it has 307 $\times$ 241 pixels in 154 spectral bands, where the major changes are crop growth situation and the water content of crops being affected by irrigation conditions in the farmland.

B. Quantitative Assessment

As change detection is a binary classification task, the overall accuracy (OA), average accuracy (AA), and the Kappa coefficient (KP) were used for quantitative performance assessment. OA is the percentage of correctly classified pixels, which is defined by

$$\text{OA} = \frac{TP + TN}{TP + TN + FP + FN} \tag{7}$$

where TP, TN, FP, and FN denote the correctly detected changed pixels, correctly detected unchanged pixels, incorrectly detected changed pixels, and incorrectly detected unchanged pixels, respectively.

KP is to measure the interrater reliability that represents the degree of similarity between the change map and the ground truth defined as follows:

$$\text{KP} = \frac{OA - PRE}{1 - PRE} \tag{8}$$

$$\text{PRE} = \frac{(TP + FP)(TP+FN) + (FN+TN)(FP+TN)}{(TP + TN + FP + FN)^2}. \tag{9}$$

AA is the average classification accuracy of the two classes, defined by

$$\text{AA} = \left(\frac{TP}{TP + FP} + \frac{TN}{TN + FN}\right)/2. \tag{10}$$

Precision (Pre) describes how many of the changed pixels detected by the method are accurate, defined by

$$\mathrm{Pre} = \frac{TP}{TP + FP}. \tag{11}$$

Recall (Re) represents how many of the actual changed pixels have been correctly detected.

$$\mathrm{Re} = \frac{TP}{TP + FN}. \tag{12}$$

F1 score (F1) defines a balanced index that can be considered as harmonic mean of Pre and Re.

$$\mathrm{F1} = 2 * \frac{\mathrm{Pre} * \mathrm{Re}}{\mathrm{Pre} + \mathrm{Re}}. \tag{13}$$

C. Results and Analysis

To evaluate the efficacy of the proposed ABBD, we compare it with some classic unsupervised HCD methods, including image algebraic-based ones such as absolute distance (AD) [43], CVA [10] and SAM [11], image transform-based, e.g., PCA-KM [13], IR-MAD [15], and DTW-KM [12], and hybrid methods, e.g., Patch tensor-based HCD (PTCD) [44], Spectral angle weighted local AD (SALA) [45], and three-order Tucker decomposition and reconstruction detector (TDRD) [16]. A brief of these selected approaches is given as follows.

1) AD [43]: The absolute difference between spectral values is accumulated as the change map, followed by *k*-means binary classification.
2) CVA [10]: The Euclidean distance between two spectral pixels is used to decide the change map, followed by *k*-means binary classification.
3) SAM [11]: The angle between the two spectral vectors is employed to determine the change map.
4) PCA-KM [13]: With PCA to reduce the data dimension and redundancy, followed by *k*-means clustering for binary classification of changed pixels.
5) IR-MAD [15]: By extracting altered objects via canonical correlation analysis to amplify the variance of independently transformed variables, it iterates the weights of distinct observations, assigning larger weights to those with fewer changes and vice versa.
6) DTW-KM [12]: It gauges the similarity between two spectral vectors by calculating the minimum cumulative distance of corresponding pixels across all spectral bands.
7) PTCD [44]: Unsupervised tensor-based method, it utilizes tensor decomposition and reconstruction to mitigate the impact of various factors in bitemporal images, incorporating a patch-based approach to leverage spatial structural information by considering nonoverlapping local similarities.
8) SALA [45]: Spectral angle weighted local AD is used to reconstruct a discriminative feature for robustness.
9) TDRD [16]: After addressing the impact of diverse factors via Tucker decomposition and reconstruction, it employs the singular value accumulation to identify key components in factor matrices and utilizes spectral angle analysis to assess spectral changes across different domains, thereby capturing both the spectral and spatial information.

TABLE I
COMPARISONS BETWEEN ABBD AND VARIOUS UNSUPERVISED METHODS ON THE RIVER DATASET

Method	OA (%)	KP	AA (%)	Pre	Re	F1
AD	94.3092	0.7137	94.6912	0.6108	0.9515	0.7440
CVA	92.5293	0.6528	94.2577	0.5393	0.9635	0.6915
SAM	96.3041	0.7326	81.8914	0.9024	0.6445	0.7519
PCA-KM	95.1686	0.7478	**95.1199**	0.6524	0.9506	0.7738
IR-MAD	94.4391	0.6745	86.2955	0.7644	0.6541	0.7050
DTW-KM	96.0066	0.7095	80.7302	**0.8837**	0.6224	0.7304
PTCD	71.1103	0.2638	82.6174	0.2269	**0.9655**	0.3675
TDRD	92.3142	0.6336	92.4186	0.5333	0.9254	0..6767
SALA	91.4629	0.6146	92.8807	0.5047	0.9460	0.6582
ABBD	**96.3758**	**0.7928**	93.6957	0.7377	0.9045	**0.8126**

Our results are bolded.

For quantitative assessments, the OA, AA, and KP on the three datasets are compared in Table I, which have clearly shown the superiority of ABBD in all three metrics. The highest results averaged on all datasets have validated the superiority of ABBD, thanks to the binary distancing the parameter-free implementation. Detailed analysis and visual comparison of the detected change maps for each dataset are detailed below. In the change maps shown in Figs. 4–6, white and black areas denote the correctly detected changed and unchanged pixels, whilst the false alarms and missing pixels are marked in red and green, respectively.

1) Results on the River Dataset: For the River dataset, Table I presents the indices describing the binary classification accuracy of all unsupervised methods. ABBD has produced the highest OA and KP values within the group, although the AA is slightly lower than the highest one derived from PCA-KM. As seen in the detected change maps in Fig. 5, ABBD has missed some small objects to the bottom-right side of the image than the PCA-KM, though the latter seems to have more false detection.

In addition, algebraic-based methods have the worse results, which has been significantly improved by the transformation-based approaches, especially for detection of large changed areas, mainly due to their inclusion of global spatial information. However, image-transformation based approaches fail to perform well in detecting the subtle sporadic changing pixels, leading to a high false alarm rate. For ABBD, it demonstrates a well-balanced detection of the changed and unchanged regions. Even without the spatial information, ABBD still outperforms all others in terms of OA and KP, the achieved KP at 0.7928 surpassing the next one by 0.0602.

2) Results on the Yancheng Dataset: For the Yancheng dataset, the extracted change maps are compared in Fig. 6 and the quantitative assessment results are shown in Table II. As seen, all algebra-based methods, including CVA, AD, SAM, and DTW-KM, yield poor outcomes with many missing detected pixels, leading to low values of OA (less than 88%) and KP (less than 0.71). In contrast, PTCD achieved the highest KP among unsupervised methods, as the spatial information used

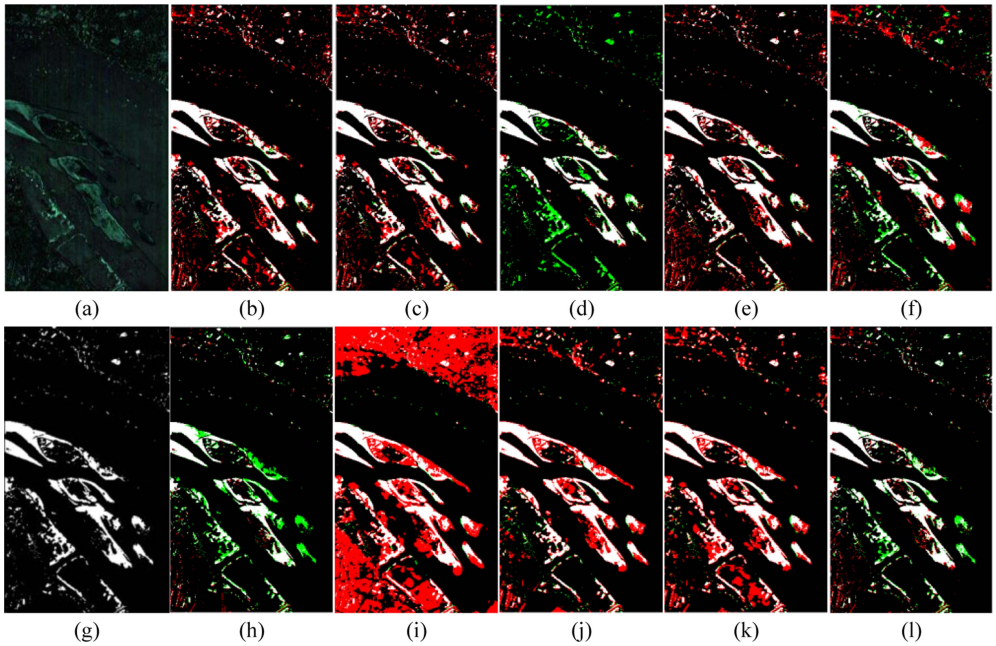

Fig. 5. Extracted change maps on the River dataset from different methods of (b) AD; (c) CVA; (d) SAM; (e) PCA; (f) IR-MAD; (h) DTW-KM; (i) PTCD; (j) TDRD; (k) SALA and (l) our ABBD in comparison to the pseudocolor image of the difference between (a) bitemporal images and (g) the ground-truth map, where the false alarms and missing pixels are labeled in red and green, respectively.

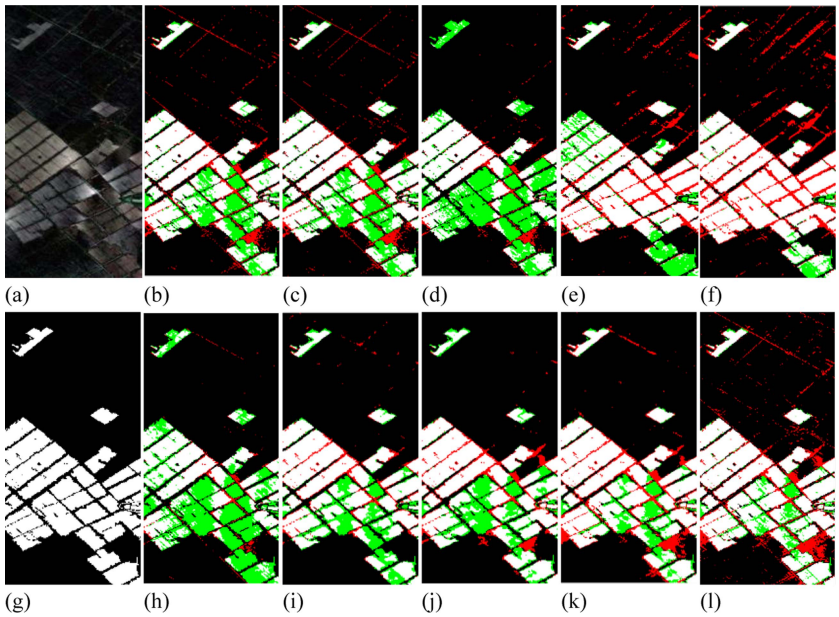

Fig. 6. Extracted change maps on the Yancheng dataset from different methods of (b) AD; (c) CVA; (d) SAM; (e) PCA; (f) IR-MAD; (h) DTW-KM; (i) PTCD; (j) TDRD; (k) SALA; and (l) our ABBD in comparison to the pseudocolor image of the difference between (a) bitemporal images and (g) the ground-truth map, where the false alarms and missing pixels are labeled in red and green, respectively.

has improved the detection of intermediate regions. However, some nonchanging pixels situated in the middle of the visual map are misclassified, leading to an increased false alarm. This drawback prevents the accurate separation of the boundaries of each changing area, which could potentially affect the precision of the results.

Similar to other methods, ABBD has the second highest values of OA and KP, lower than PTCD by 0.0129 in KP, but the missing pixels in the middle part are the least. The values of *AA* and Re are the highest among all benchmarks. Overall, these again highlight the efficacy of ABBD.

3) Results on the Hermiston Dataset: For the Hermiston dataset, the visualized results are shown and compared in Fig. 7 and the quantitative assessment results are shown in Table III. The four algebraic-based methods still perform the worst, especially the SAM. Among image-transform based methods,

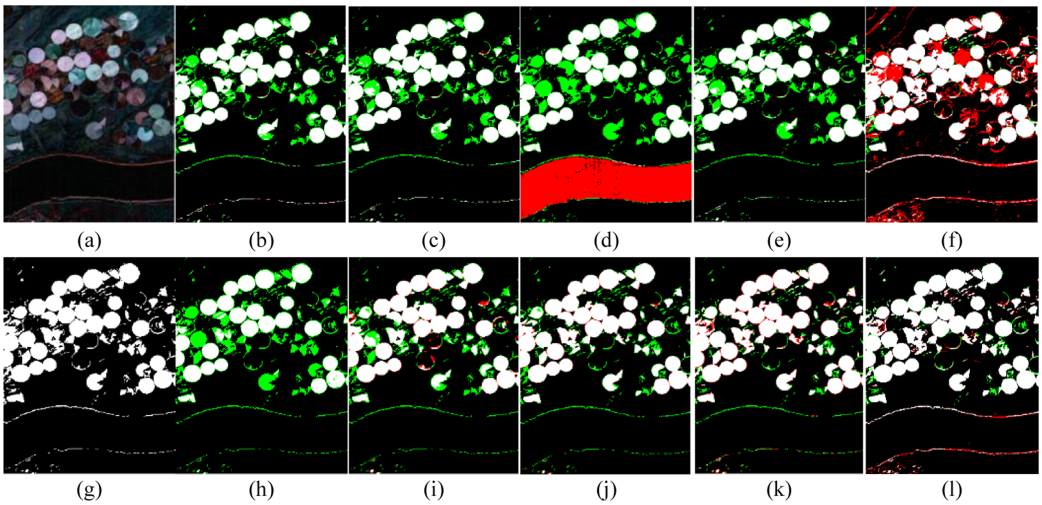

Fig. 7. Extracted change maps on the Hermiston dataset from different methods of (b) AD; (c) CVA; (d) SAM; (e) PCA; (f) IR-MAD; (h) DTW-KM; (i) PTCD; (j) TDRD; (k) SALA; and (l) our ABBD in comparison to the pseudocolor image of the difference between (a) bitemporal images and (g) the ground-truth map, where the false alarms and missing pixels are labeled in red and green, respectively.

TABLE II
COMPARISONS BETWEEN ABBD AND VARIOUS UNSUPERVISED METHODS ON THE YANCHENG DATASET

Method	OA (%)	KP	AA (%)	Pre	Re	F1
AD	87.8027	0.7074	84.2977	0.8430	0.7494	0.7935
CVA	87.5459	0.7025	84.2058	0.8327	0.7529	0.7908
SAM	82.9694	0.5558	74.7914	0.8767	0.5297	0.6604
PCA-KM	88.2789	0.7180	84.7108	0.8557	0.7519	0.8004
IR-MAD	88.7007	0.7388	87.1766	0.8119	0.8311	0.8214
DTW-KM	83.1992	0.5559	74.4774	**0.9113**	0.5122	0.6558
PTCD	**89.9031**	**0.7556**	86.3193	0.8945	0.7676	**0.8261**
TDRD	88.1735	0.7163	84.7379	0.8494	0.7557	0.7998
SALA	88.6412	0.7378	87.1896	0.8092	0.8332	0.8210
ABBD	88.7908	0.7427	**87.6470**	0.8053	**0.8459**	0.8251

Our results are bolded.

TABLE III
COMPARISONS BETWEEN ABBD AND VARIOUS UNSUPERVISED METHODS ON THE HERMISTON DATASET

Method	OA (%)	KP	AA (%)	Pre	Re	F1
AD	93.4146	0.7904	85.5461	0.9941	0.7122	0.8298
CVA	92.8663	0.7705	84.2897	0.9953	0.6867	0.8127
SAM	72.0397	0.2888	66.2565	0.4112	0.5573	0.4733
PCA-KM	92.2378	0.7472	82.8444	0.9973	0.6574	0.7924
IR-MAD	89.7509	0.6533	77.6549	0.9806	0.5563	0.7099
DTW-KM	90.2834	0.6716	78.4514	**0.9997**	0.5691	0.7253
PTCD	94.2030	0.8226	88.4859	0.9536	0.7808	0.8586
TDRD	95.8817	0.8765	91.8463	0.9683	0.8450	0.9024
SALA	96.0128	0.8843	93.6210	0.9277	0.8927	0.9098
ABBD	**97.4874**	**0.9281**	**96.4372**	0.9434	**0.9453**	**0.9443**

Our results are bolded.

PCA detected a considerable number of missing pixels, whereas IR-MAD had more false alarms.

Three advanced unsupervised algorithms, PTCD, TDRD, and SALA, have shown significantly superior performance on this dataset compared to image-algebra and image-transform based methods. Notably, the SALA outperformed all others except ABBD with an OA of 96.0115% and a KP value of 0.8842. For our ABBD, it was the best among all compared methods, with an OA of 97.4874%, a KP of 0.9281 and the AA of 96.4372%, all the highest, to confirm again the superiority of our ABBD in HCD.

4) Further Discussions of the Quantitative Results: Overall, the quantitative assessment results across three datasets shed light on the strengths and weaknesses of various unsupervised methods for HCD. One notable observation is that isolated pixels pose a significant challenge for image-transformation and tensor-based methods. Relying heavily on spatial features, it makes these approaches less effective in dealing with isolated pixels that exhibit changes, leading to high false alarms when the neighboring pixels were considered. Consequently, the detection accuracy of PCA-KM and IR-MAD is not as high as that of image-algebraic methods on datasets with a substantial number of isolated changing pixels.

On the contrary, the relatively poorer results of ABBD on the Yancheng dataset is primarily due to the following reasons: 1) as seen from the GT map, the changed areas in the Yancheng dataset are all connected large blocks, rather than loosely distributed in the other two images, the accurate classification of unchanged pixels within the blocks and the pixels along the edges of the blocks poses a challenge for this dataset; 2) and as shown in the pseudocolor image of the difference image, many dark areas in the blocks mean that there are subtle changes marked as changes, where the edges of each block in the upper right corner are marked as unchanged even they appear very bright. These are the challenges of the dataset itself that presents to the detection accuracy of unsupervised algorithms. From the comparison of

TABLE IV
COMPUTATIONAL COMPLEXITY OF OUR ABBD AND THE CLASSIC UNSUPERVISED HCD METHODS

	AD	CVA	SAM	PCA-KM	IR-MAD
Parameters	0	0	0	1	3
Complexity	$O(L*B)$	$O(L*B)$	$O(L*B)$	$O(L*B^2+B^3+LBp)$	$O(L*B^2+L*B^3)$
Computation time (s)	*1.0463*	*1.0650*	*1.7159*	*1.9782*	*3.5046*
	DTW-KM	**PTCD**	**TDRD**	**SALA**	**ABBD**
Parameters	0	2	1	0	0
Complexity	$O(L*B^2+L)$	$O(L*S^2*B+L^3)$	$O(L*B^3+L*B)$	$O(L*B)$	$O(N*L*B)$
Computation time (s)	*1.7601*	*56.4090*	*29.6332*	*1.2889*	*1.1912 (N = 1)*

Note: L, B, and p denote, respectively, the total number of pixels, the number of spectral bands, and the number of principal components used for dimension reduction; N is the number of iterations and S is the patch sizes, respectively.

visual maps, like other image algebra-based methods, the ABBD method generates a significant number of false positives in the top right corner. This is because these methods do not consider spatial features, resulting in less effective handling of edge regions compared to methods based on image transformations, such as PCA-KM and PTCD methods. However, compared to image algebra-based methods, ABBD handles subtle changes in pixels within connected blocks quite well, accurately detecting subtle changes. It is evident that ABBD's missing pixel count is much lower than other unsupervised algorithms'. This is why ABBD's detection accuracy is significantly better than other algebraic-based methods, although it is slightly inferior to image transformation-based methods.

As for other advanced methods, e.g., PTCD, TDRD, and SALA, they significantly outperform conventional unsupervised algorithms on the Yancheng and Hermiston datasets though the robustness is relatively poor. Moreover, their performance on the River dataset is notably deficient, falling below the performance of all benchmark tests.

As an unsupervised method based on image algebra without considering the spatial information, ABBD has produced significantly improved results in quantitative assessment across all three datasets. This is mainly due to the proposed binary distancing and parameter-free decision-making to mitigate the measurement inconsistency in handling both subtle and obvious spectral changes. The hightest averaged OA, KP, and AA have fully validated its efficacy in HCD, especially when processing datasets with a large number of isolated changing pixels.

As shown in Figs. 5–7(b) and (c), image algebra-based methods such as AD and CVA that use the absolute difference to measure the degrees of changes tend to produce a much higher level of false alarms than ABBD. This is mainly owing to the proposed binary distancing, which has successfully mitigated the adverse effect of noise-induced inconsistency of measurement and resulted in a significant reduction of false alarms. Along with the *k*-means based binary classification on the cumulated band-wise binary change map, more accurate and robust HCD has been achieved on all the three datasets.

IV. DISCUSSION

To comprehensively validate the effectiveness of our proposed method, we conduct a series of experiments covering computational complexity, threshold adaptive iteration, classifier selection, and comparison with results obtained from advanced DL-based algorithms.

A. Computational Complexity Analysis

Herein, we analyze the computational complexity of all unsupervised methods briefly in Table IV, where L denotes the total number of pixels ($L = W*H$), p is the number of the principal components for dimension reduction, S is the patch size, and N represents the number of iterations.

In general, algebraic operations are much simpler than image-transformation based ones. AD, CVA SAM, and SALA have the least computational complexity because they rely on the pixel-wise difference between the spectral vectors. Due to the need for sequence alignment in the spectral domain, DTW-KM has a much higher computational complexity.

For the image-transformation based methods, such as PCA and IR-MAD, their computational complexity is much larger than the algebraic operations, due to the need to calculate the difference or correlation in the transformed domain. PTCD involves the segmentation of the HSI into different patches before applying feature extraction on the constructed tensor. TDRD requires a three-order Tucker decomposition of the high-dimensional HSI, followed by feature extraction from the core tensor or mode matrices. In addition, it needs to reconstruct the detected change regions from the feature space back to the original image space. Consequently, these two methods are most complex within the group. For ABBD, it has the same lowest computational complexity as the image-algebraic methods when ε is set to a fixed value ($N = 1$). With the increasing of iterations, the computational cost of ABBD will grow linearly. We have also compared the computation times of all algorithms on River dataset, which are summarized in Table II. All algorithms were executed based on MATLAB on an NVIDIA RTX A2000, and their parameters were set according to the specifications provided in the original paper. To ensure experimental fairness, the computation time reported only includes the runtime of the algorithms and excludes data loading time. From the comparison result, it can be observed that methods based on algebraic operations generally require significantly less time compared to those based on image transformations. For ABBD, it also has similar runtime compared to other algebraic-based methods when ε is set to a fixed value ($N = 1$). However, as N increases,

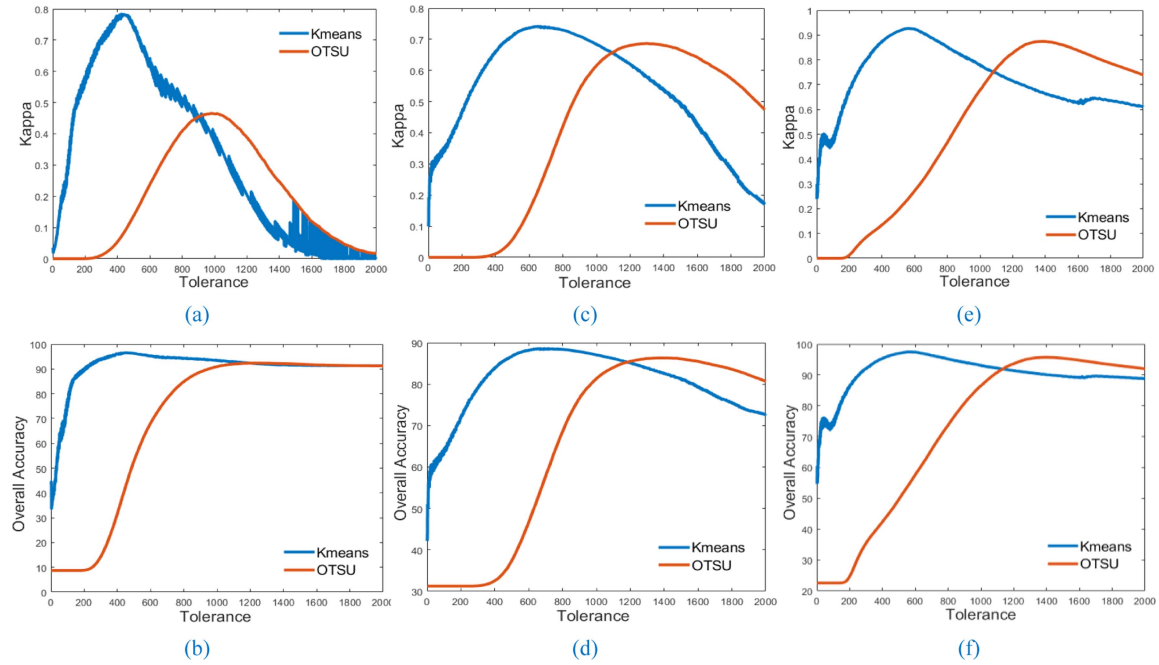

Fig. 8. Variation comparison under different values ε: KP on the (a) River; (c) Yancheng; and (e) Hermiston dataset; and OA comparison on the (b) River; (d) Yancheng; and (f) Hermiston.

the runtime will grow linearly. How to reduce the number of loops based on the determined N will be further investigated.

In addition, the number of control parameters in these approaches is analyzed for comparison. Image algebra-based methods, including AD, CVA, SAM, and SALA, inherently extract and compare spectral differences, obviating the need for control parameters. On the contrary, image transformation-based methods exhibit varying sensitivities to the parameter settings. Specifically, PCA-KM's detection outcomes depend on the number of principal components used, while IR-MAD is impacted by three key parameters: 1) the maximum number of iterations; 2) thresholds; and 3) the penalty terms. PTCD's detection accuracy hinges on factors such as the window size and interblock stride, while TDRD's performance is affected by the rate parameter between bi-temporal images. Thanks for the capability embedded within the ABBD that can automatically determine the associated parameters. This has enabled ABBD as a parameter-free solution for extra robustness and ease of deployment whilst producing high accuracy results of HCD.

B. Effect of Binary K-Means versus Thresholding

Based on the accumulated change map, there are two ways to make the final binary decision in HCD, i.e., k-means clustering and thresholding, while maintaining the parameter ε spanning within [1, 2000] to explore the full range of the variations. The corresponding results on the three datasets are given in Fig. 8, where OTSU was used to determine the optimal threshold for the accumulated change map at each ε. As seen, all the KP and OA curves exhibited an initial ascent followed by a decline as ε increases. This is due to the fact that a larger ε will put a higher threshold to detect changed pixels. In other words, it will result in more missing detection hence the declined KP towards zero along with a stabilized OA.

TABLE V
RESULTS OF USING A FIXED TOLERANCE THRESHOLD

	River		Yancheng		Hermiston	
	k-means	OTSU	k-means	OTSU	k-means	OTSU
OA (%)	96.5398	92.3621	88.6497	86.3452	97.4631	95.7128
KP	0.7791	0.4713	0.7383	0.6868	0.9269	0.8747
Optimal ε	453	981	679	1300	569	1385

It is worth highlighting that k-means consistently outperformed OTSU thresholding in both the KP and OA. The optimal ε for k-means turned out to be considerably smaller than that for OTSU. This finding underscores the efficiency advantage of k-means clustering over OTSU thresholding while delivering superior results of HCD. Hence, in the ultimate selection of the binary classifier, we opted for the k-means clustering. In addition, quantitative assessment is summarized in Table V. As seen, the maximum KP achieved by thresholding with a fixed ε falls short of the k-means binary classification, as seen in Table III, indicating the efficacy of k-means versus thresholding.

C. Effect of the Adaptively Determined Optimal N

From (4), ABBD can automatically derive the optimal values of N as 1055, 1319, and 978 for the three datasets of the River, Yancheng, and Hermiston, respectively. In addition, to further validate the efficacy of the automatically determined parameter N, we compare the detection results from this N with those

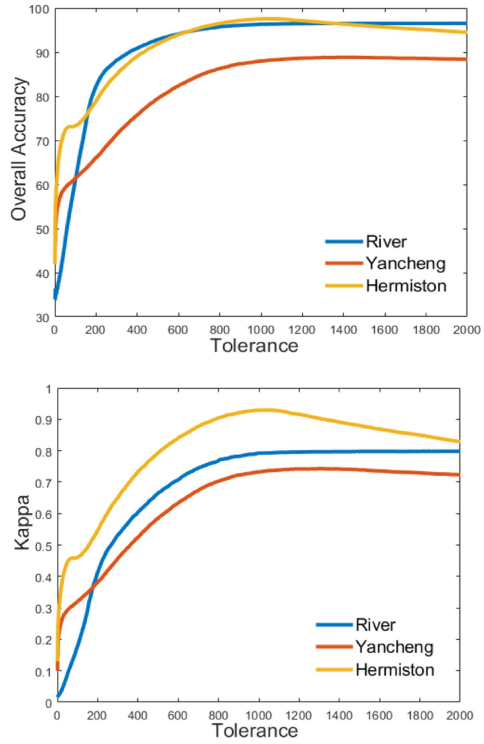

Fig. 9. Results of the OA and KP versus an increasing N.

TABLE VI
RESULTS UNDER MANUALLY AND AUTOMATICALLY DETERMINED VALUES OF N

	River		Yancheng		Hermiston	
	Manual	Auto	Manual	Auto	Manual	Auto
N	1999	1055	1296	1319	1053	978
OA	0.9654	0.9638	0.8884	0.8879	0.9757	0.9749
KP	0.7981	0.7928	0.7433	0.7427	0.9296	0.9281

manually determined optimal values of N according to the best detection accuracy, as shown in Fig. 9. Note that the manually determined values of N are 1999, 1296, and 1053, in comparison to the automatically derived values of 1055, 1319, and 978 from the three datasets of River, Yancheng and Hermiston, respectively. The OA and KP yielded on the three datasets, using both the manually and automatically determined N, and are compared in Table VI. Although the N values can be much different, the produced OA and KP are very close to each other, which has validated the efficacy of the adaptive solution in determining the N.

Interestingly, the comparison of results revealed that the OA and KP values attained at the optimal N values were slightly improved when compared to the adaptively determined N, although the differences were relatively small. This outcome further validates the efficacy of our ABBD in determining the appropriate N values for the iterative process and achieve truly parameter-free unsupervised HCD that is applicable to different datasets.

TABLE VII
COMPARING ABBD WITH SUPERVISED DEEP LEARNING METHODS

Models	Train ratio	River		Yancheng		Hermiston	
		OA	KP	OA	KP	OA	KP
3-D CNN	5%	0.9601	0.7364	0.9558	0.8977	0.9505	0.8588
2-D CNN		0.9579	0.7261	0.9497	0.8839	0.9443	0.8375
CSA Net		0.9670	0.7786	0.9619	0.9112	0.9547	0.8638
CBA Net		0.9609	0.7518	0.9601	0.9068	0.9673	0.9045
ABBD	**0%**	**0.9638**	**0.7920**	**0.8878**	**0.7418**	**0.9749**	**0.9288**
3-D CNN	10%	0.9647	0.7706	0.9649	0.9183	0.9575	0.8803
2-D CNN		0.9644	0.7661	0.9591	0.9050	0.9486	0.8490
CSA Net		0.9706	0.8128	0.9692	0.9290	0.9512	0.8661
CBA Net		0.9769	0.8344	0.9657	0.9213	0.9727	0.9218

Our results are bolded.

D. Compare With Supervised DL-Based Algorithms

For extended performance assessment, we compare ABBD with several supervised deep learning (DL) based models, including 2-D CNN [46], 3-D CNN [47], CSANet [48], and CBANet [5]. We conducted the training using two distinct subsets, i.e., 5% and 10% of the labeled pixels, respectively, while using the remaining for testing. The training samples were randomly selected each time, and the averaged OA and KP in three runs were used for comparison, as shown in Table VII.

For the River dataset, with a training ratio of 5%, ABBD outperformed all DL models in both OA and KP. When increasing the training ratio to 10%, ABBD was beaten by CBANet and CSANet, though it has comparable or even slightly better results than 3-D CNN and 2-D CNN, especially in KP. For the Yancheng dataset, irrespective of using 5% or 10% of pixels for training, all DL-based models surpass ABBD and other unsupervised methods by a large margin. This was due to the removal of a large number of noisy bands from the dataset, resulting in weakened representation of the handcrafted features hence the low detection accuracy of the unsupervised algorithms [49]. For the Hermiston dataset, ABBD outperforms all DL-based methods in both OA and KP when the training ratio is up to 10%.

ABBD has shown much worse results on the Yancheng dataset than the River and Hermiston, which can be explained as follows. In both the River and Hermiston datasets, the changed areas include a complex landscape of interconnected regions and numerous isolated pixels. Addressing the distinctions among these isolated pixels in the spectral domain is the strength of ABBD. Thanks to the proposed binary distancing and adaptive solution, ABBD outperforms those that solely rely on spatial characteristics and neglect the pixel-level spectral features, such as 2-D CNN, 3-D CNN, and CSANet, as they focus on image-level operations to exploit the spatial correlation [50]. Therefore, they show remarkable detection accuracy when handling changed pixels within connected regions on both datasets, but not the isolated small regions. This also explains why these models exhibited clear advantages of better results when applied to

the Yancheng dataset, which contained a substantial number of interconnected areas of changes. On the contrary, CBANet's proficiency in addressing isolated pixels of changes becomes more pronounced as it leverages 1×1 convolutional layers to consider pixel-level spectral features, which amplifies with an increasing training ratio. As changed regions can be of various sizes, this has shown the value and importance of both spectral and spatial features in HCD when applying different approaches including DL.

V. Conclusion

In this article, we have proposed a novel method, ABBD for unsupervised parameter-free hyperspectral change detection. The proposed four strategies have helped to significantly improve the efficiency and robustness of ABBD in HCD. First, band-wise binary distancing can successfully mitigate the measurement inconsistency. Second, it is found that the *k*-means used for binary decision-making has surpassed thresholding using OTSU. Third, the adaptive solution is found particularly useful in automatically determining the parameter *N* for achieving a fully parameter-free approach in HCD. With these strategies, ABBD has outperformed a number of state-of-the-art approaches including several deep learning models when the training ratio is relatively low.

While promising, there remains space for further improvement. First, the detection accuracy can be further improved by incorporating spatial-spectral information, spatial-contextual information [19], and ways of sample enhancement [51], though at an increased computational cost. Second, advanced clustering algorithms, e.g., matrix factorization-based and graph learning-based incomplete multiview clustering methods [52] can be applied to replace *k*-means to handle more complex cluster distributions. Finally, testing on a more diverse set of HSI datasets, including cross-sensor and cross-domain examples, would be beneficial to validate the generalizability of ABBD.

References

[1] G. Sun et al., "Deep fusion of localized spectral features and multi-scale spatial features for effective classification of hyperspectral images," *Int. J. Appl. Earth Observ. Geoinf.*, vol. 91, 2020, Art. no. 102157.

[2] G. Sun et al., "Combinational shadow index for building shadow extraction in urban areas from Sentinel-2A MSI imagery," *Int. J. Appl. Earth Observ. Geoinf.*, vol. 78, pp. 53–65, 2019.

[3] Y. Yan et al., "Non-destructive testing of composite fiber materials with hyperspectral imaging—Evaluative studies in the EU H2020 FibreEUse project," *IEEE Trans. Instrum. Measur.*, vol. 71, 2022, Art. no. 6002213.

[4] G. Sun et al., "Stratified spectral mixture analysis of medium resolution imagery for impervious surface mapping," *Int. J. Appl. Earth Observ. Geoinf.*, vol. 60, pp. 38–48, 2017.

[5] Y. Li, J. Ren, Y. Yan, and A. Petrovski, "CBANet: An end-to-end cross Band 2-D attention network for hyperspectral change detection in remote sensing," *IEEE Trans. Geosci. Remote Sens.*, vol. 61, 2023, Art. no. 5513011.

[6] X. Zheng, X. Chen, X. Lu, and B. Sun, "Unsupervised change detection by cross-resolution difference learning," *IEEE Trans. Geosci. Remote Sens.*, vol. 60, 2021, Art. no. 5606616.

[7] N. Zhang et al., "A review of advanced technologies and development for hyperspectral-based plant disease detection in the past three decades," *Remote Sens.*, vol. 12, no. 19, 2020, Art. no. 3188.

[8] S. Liu, D. Marinelli, L. Bruzzone, and F. Bovolo, "A review of change detection in multitemporal hyperspectral images: Current techniques, applications, and challenges," *IEEE Geosci. Remote Sens. Mag.*, vol. 7, no. 2, pp. 140–158, Jun. 2019.

[9] K. L. Ang and J. K. P. Seng, "Big data and machine learning with hyperspectral information in agriculture," *IEEE Access*, vol. 9, pp. 36699–36718, 2021.

[10] W. A. Malila, "Change vector analysis: An approach for detecting forest changes with landsat," in *LARS Symposia*, 1980, Art. no. 385.

[11] S. Kuching, "The performance of maximum likelihood, spectral angle mapper, neural network and decision tree classifiers in hyperspectral image analysis," *J. Comput. Sci.*, vol. 3, no. 6, pp. 419–423, 2007.

[12] O. Csillik, M. Belgiu, G. P. Asner, and M. Kelly, "Object-based time-constrained dynamic time warping classification of crops using Sentinel-2," *Remote Sens.*, vol. 11, no. 10, Art. no. 1257, 2019.

[13] M. Hasanlou and S. T. Seydi, "Hyperspectral change detection: An experimental comparative study," *Int. J. Remote Sens.*, vol. 39, no. 20, pp. 7029–7083, 2018.

[14] A. A. Nielsen, K. Conradsen, and J. J. Simpson, "Multivariate alteration detection (MAD) and MAF postprocessing in multispectral, bitemporal image data: New approaches to change detection studies," *Remote Sens. Environ.*, vol. 64, no. 1, pp. 1–19, 1998.

[15] A. A. Nielsen, "The regularized iteratively reweighted MAD method for change detection in multi-and hyperspectral data," *IEEE Trans. Image Process.*, vol. 16, no. 2, pp. 463–478, Feb. 2007.

[16] Z. Hou, W. Li, R. Tao, and Q. Du, "Three-order Tucker decomposition and reconstruction detector for unsupervised hyperspectral change detection," *IEEE J. Sel. Topics Appl. Earth Observ. Remote Sens.*, vol. 14, pp. 6194–6205, 2021.

[17] D. Marinelli, F. Bovolo, and L. Bruzzone, "A novel change detection method for multitemporal hyperspectral images based on binary hyperspectral change vectors," *IEEE Trans. Geosci. Remote Sens.*, vol. 57, no. 7, pp. 4913–4928, Jul. 2019.

[18] H. Chen et al., "Change detection based on difference image and energy moments in remote sensing image monitoring," *Pattern Recognit. Image Anal.*, vol. 28, pp. 273–281, 2018.

[19] Z. Lv, M. Zhang, W. Sun, and J. A. Benediktsson, "Spatial-contextual information utilization framework for land cover change detection with hyperspectral remote sensed images," *IEEE Trans. Geosci. Remote Sens.*, vol. 61, 2023, Art. no. 4411911.

[20] S. Saha, F. Bovolo, and L. Bruzzone, "Unsupervised deep change vector analysis for multiple-change detection in VHR images," *IEEE Trans. Geosci. Remote Sens.*, vol. 57, no. 6, pp. 3677–3693, Jun. 2019.

[21] B. Yang, Y. Mao, L. Liu, X. Liu, Y. Ma, and J. Li, "From trained to untrained: A novel change detection framework using randomly initialized models with spatial–channel augmentation for hyperspectral images," *IEEE Trans. Geosci. Remote Sens.*, vol. 61, 2023, Art. no. 4402214.

[22] S. Saha, L. Kondmann, Q. Song, and X. X. Zhu, "Change detection in hyperdimensional images using untrained models," *IEEE J. Sel. Topics Appl. Earth Observ. Remote Sens.*, vol. 14, pp. 11029–11041, 2021.

[23] Q. Li, T. Mu, A. Tuniyazi, Q. Yang, and H. Dai, "Progressive pseudo-label framework for unsupervised hyperspectral change detection," *Int. J. Appl. Earth Observ. Geoinf.*, vol. 127, 2024, Art. no. 103663.

[24] M. Hu, C. Wu, B. Du, and L. Zhang, "Binary change guided hyperspectral multiclass change detection," *IEEE Trans. Image Process.*, vol. 32, pp. 791–806, 2023.

[25] M. Ahangarha, S. T. Seydi, and R. Shahhoseini, "Hyperspectral change detection in wetland and water-body areas based on machine learning," *Int. Arch. Photogram., Remote Sens. Spatial Inf. Sci.*, vol. 42, pp. 19–24, 2019.

[26] S. Liu, Q. Du, X. Tong, A. Samat, H. Pan, and X. Ma, "Band selection-based dimensionality reduction for change detection in multi-temporal hyperspectral images," *Remote Sens.*, vol. 9, no. 10, 2017, Art. no. 1008.

[27] L. Mou, L. Bruzzone, and X. X. Zhu, "Learning spectral-spatial-temporal features via a recurrent convolutional neural network for change detection in multispectral imagery," *IEEE Trans. Geosci. Remote Sens.*, vol. 57, no. 2, pp. 924–935, Feb. 2019.

[28] Q. Wang, Z. Yuan, Q. Du, and X. Li, "GETNET: A general end-to-end 2-D CNN framework for hyperspectral image change detection," *IEEE Trans. Geosci. Remote Sens.*, vol. 57, no. 1, pp. 3–13, Jan. 2019.

[29] M. Hu, C. Wu, and L. Zhang, "HyperNet: Self-supervised hyperspectral spatial–spectral feature understanding network for hyperspectral change detection," *IEEE Trans. Geosci. Remote Sens.*, vol. 60, 2022, Art. no. 5543017.

[30] T. Zhan et al., "TDSSC: A three-directions spectral–spatial convolution neural network for hyperspectral image change detection," *IEEE J. Sel. Topics Appl. Earth Observ. Remote Sens.*, vol. 14, pp. 377–388, 2021.
[31] F. Luo, T. Zhou, J. Liu, T. Guo, X. Gong, and J. Ren, "Multiscale diff-changed feature fusion network for hyperspectral image change detection," *IEEE Trans. Geosci. Remote Sens.*, vol. 61, 2023, Art. no. 5502713.
[32] Z. Lv, J. Liu, W. Sun, T. Lei, J. A. Benediktsson, and X. Jia, "Hierarchical attention feature fusion-based network for land cover change detection with homogeneous and heterogeneous remote sensing images," *IEEE Trans. Geosci. Remote Sens.*, vol. 61, 2023, Art. no. 4411115.
[33] Y. Wang, J. Sha, L. Gao, Y. Zhang, X. Rong, and C. Zhang, "A semi-supervised domain alignment transformer for hyperspectral images change detection," *IEEE Trans. Geosci. Remote Sens.*, vol. 61, 2023, Art. no. 5525411.
[34] C. Zhou, Q. Shi, D. He, B. Tu, H. Li, and A. Plaza, "Spectral-spatial sequence characteristics-based convolutional transformer for hyperspectral change detection," *CAAI Trans. Intell. Technol.*, vol. 8, no. 4, pp. 1237–1257, 2023.
[35] B. Tu, Q. Ren, J. Li, Z. Cao, Y. Chen, and A. Plaza, "NCGLF2: Network combining global and local features for fusion of multisource remote sensing data," *Inf. Fusion*, vol. 104, 2024, Art. no. 102192.
[36] C. Zhou, Z. He, A. Lou, and A. Plaza, "RGB-to-HSV: A frequency-spectrum unfolding network for spectral super-resolution of RGB videos," *IEEE Trans. Geosci. Remote Sens.*, vol. 62, 2024, Art. no. 5609318.
[37] L. Khelifi and M. Mignotte, "Deep learning for change detection in remote sensing images: Comprehensive review and meta-analysis," *IEEE Access*, vol. 8, pp. 126385–126400, 2020.
[38] R. C. Veltkamp, "Shape matching: Similarity measures and algorithms," in *Proc. Int. Conf. Shape Model. Appl.*, 2001, pp. 188–197.
[39] Q. Guo, J. Zhang, and Y. Zhang, "Multitemporal hyperspectral images change detection based on joint unmixing and information coguidance strategy," *IEEE Trans. Geosci. Remote Sens.*, vol. 59, no. 11, pp. 9633–9645, Nov. 2021.
[40] M. T. Eismann, J. Meola, and R. C. Hardie, "Hyperspectral change detection in the presence of diurnal and seasonal variations," *IEEE Trans. Geosci. Remote Sens.*, vol. 46, no. 1, pp. 237–249, Jan. 2008.
[41] K. P. Sinaga and M.-S. Yang, "Unsupervised k-means clustering algorithm," *IEEE Access*, vol. 8, pp. 80716–80727, 2020.
[42] G. Sun et al., "SpaSSA: Superpixelwise adaptive SSA for unsupervised spatial–spectral feature extraction in hyperspectral image," *IEEE Trans. Cybern.*, vol. 52, no. 7, pp. 6158–6169, Jul. 2022.
[43] P. Du, S. Liu, P. Gamba, K. Tan, and J. Xia, "Fusion of difference images for change detection over urban areas," *IEEE J. Sel. Topics Appl. Earth Observ. Remote Sens.*, vol. 5, no. 4, pp. 1076–1086, Aug. 2012.
[44] Z. Hou, W. Li, and Q. Du, "A patch tensor-based change detection method for hyperspectral images," in *Proc. IEEE Int. Geosci. Remote Sens. Symp.*, 2021, pp. 4328–4331.
[45] Z. Hou, W. Li, L. Li, R. Tao, and Q. Du, "Hyperspectral change detection based on multiple morphological profiles," *IEEE Trans. Geosci. Remote Sens.*, vol. 60, 2021, Art. no. 5507312.
[46] N. He et al., "Feature extraction with multiscale covariance maps for hyperspectral image classification," *IEEE Trans. Geosci. Remote Sens.*, vol. 57, no. 2, pp. 755–769, Feb. 2019.
[47] A. B. Hamida, A. Benoit, P. Lambert, and C. B. Amar, "3-D deep learning approach for remote sensing image classification," *IEEE Trans. Geosci. Remote Sens.*, vol. 56, no. 8, pp. 4420–4434, Aug. 2018.
[48] R. Song, W. Ni, W. Cheng, and X. Wang, "CSANet: Cross-temporal interaction symmetric attention network for hyperspectral image change detection," *IEEE Geosci. Remote Sens. Lett.*, vol. 19, 2022, Art. no. 6010105.
[49] J. Qu, S. Hou, W. Dong, Y. Li, and W. Xie, "A multilevel encoder–decoder attention network for change detection in hyperspectral images," *IEEE Trans. Geosci. Remote Sens.*, vol. 60, 2021, Art. no. 5518113.
[50] S. K. Roy, G. Krishna, S. R. Dubey, and B. B. Chaudhuri, "HybridSN: Exploring 3-D–2-D CNN feature hierarchy for hyperspectral image classification," *IEEE Geosci. Remote Sens. Lett.*, vol. 17, no. 2, pp. 277–281, Feb. 2020.
[51] Z. Lv, P. Zhang, W. Sun, T. Lei, J. A. Benediktsson, and P. Li, "Sample iterative enhancement approach for improving classification performance of hyperspectral imagery," *IEEE Geosci. Remote Sens. Lett.*, vol. 21, 2024, Art. no. 2500605.
[52] J. Wen et al., "A survey on incomplete multiview clustering," *IEEE Trans. Syst., Man, Cybern., Syst.*, vol. 53, no. 2, pp. 1136–1149, Feb. 2023.

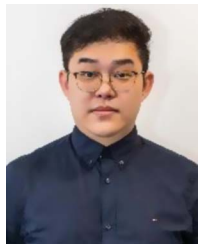

Yinhe Li received the B.E. degree in electronic and electrical engineering from Northeast Electric Power University, Jilin, China, and the University of Strathclyde, Glasgow, U.K., in 2020. He is currently working toward the Ph.D. degree in advanced processing techniques for change and anomaly detection in hyperspectral images with National Subsea Centre, Robert Gordon University, Aberdeen, U.K.

His research interests include hyperspectral imagery and deep learning.

Jinchang Ren (Senior Member, IEEE) received the B.E. degree in computer software, the M.Eng. degree in image processing, and the D.Eng. degree in computer vision from Northwestern Polytechnical University, Xi'an, China, in 1992, 1997, and 2000, respectively, and the Ph.D. degree in electronic imaging and media communication from the University of Bradford, Bradford, U.K., in 2009.

He is currently a Professor of computing with Transparent Ocean Lead, National Subsea Centre, Robert Gordon University, Aberdeen, U.K., and a Visiting Professor with Guangdong Polytechnic Normal University (GPNU), Guangzhou, China. He has authored or coauthored more than 400 peer-reviewed journal/conferences papers. His research interests include hyperspectral imaging, computer vision, Big Data analytics, and machine learning.

Dr. Ren is an Associate Editor for several international journals including IEEE TRANSACTIONS ON GEOSCIENCE AND REMOTE SENSING and *Journal of the Franklin Institute*.

Yijun Yan (Member, IEEE) received the Ph.D. degree in electrical and electronic engineering from the University of Strathclyde, Glasgow, U.K., in 2018.

He holds the position of Lecturer in computing with the University of Dundee, Dundee, U.K., alongside an honorary role as Lecturer with Robert Gordon University, Aberdeen, U.K. His research interests include pattern recognition, hyperspectral imagery, and their application in remote sensing, as well as nondestructive testing across diverse industrial environments.

Dr. Yan has contributed extensively to renowned journals such as *Pattern Recognition*, IEEE TRANSACTIONS ON INSTRUMENTATION AND MEASUREMENT, IEEE TRANSACTIONS ON GEOSCIENCE AND REMOTE SENSING, IEEE JOURNAL OF BIOMEDICAL AND HEALTH INFORMATICS, etc. He serves as a Guest Editor for *Remote Sensing* and *Frontiers in Plant Science* and is a respected Reviewer for IEEE TRANSACTIONS ON IMAGE PROCESSING, IEEE TRANSACTIONS ON GEOSCIENCE AND REMOTE SENSING, and IEEE TRANSACTIONS ON INSTRUMENTATION AND MEASUREMENT, etc.

Ping Ma received the Ph.D. degree in signal and image processing from the Department of Electronic and Electrical Engineering, University of Strathclyde, Glasgow, U.K., in 2022.

She is currently a Research Fellow with National Subsea Centre, Robert Gordon University, Aberdeen, U.K. Her research interests include multimodal remote sensing, hyperspectral imaging, and machine learning.

Maher Assaad received the master's degree in electrical engineering/microelectronics IC design from the University of Montreal, Montreal, Canada, in 2002, and the Ph.D. degree in electrical engineering/microelectronics IC design from the University of Glasgow, Glasgow, U.K., in 2009.

He was a Senior Electrical Engineering Lecturer with the University Technology of PETRONAS, Seri Iskandar, Malaysia, and an Associate Professor of electronic and communication engineering with the American University of Ras Al Khaimah, Ras Al Khaimah, UAE. He is currently a Professor of electrical and computer engineering with Ajman University, Ajman, UAE. His research interests include the design of circuits/integrated circuits for various types of sensors and wireline and optical communication systems.

Zhi Gao (Member, IEEE) received the B.E. and Ph.D. degrees from Wuhan University, Wuhan, China, in 2002 and 2007, respectively.

In 2008, he joined the Interactive and Digital Media Institute, National University of Singapore (NUS), Singapore, as a Research Fellow and a Project Manager. In 2014, he joined the Temasek Laboratories in NUS (TL@NUS), as a Research Scientist (A) and a Principal Investigator. He is currently working as a Full Professor with the School of Remote Sensing and Information Engineering, Wuhan University. He has authored or coauthored more than 90 academic articles, which have been published in *International Journal of Computer Vision* (IJCV), IEEE TRANSACTIONS ON PATTERN ANALYSIS AND MACHINE INTELLIGENCE (PAMI), International Society for Photogrammetry and Remote Sensing (ISPRS), *Journal of Photogrammetry and Remote Sensing* (JPRS), IEEE TRANSACTIONS ON GEOSCIENCE AND REMOTE SENSING, IEEE TRANSACTIONS ON INTELLIGENT TRANSPORTATION SYSTEMS (ITS), and other top journals. His research interests include computer vision, machine learning, remote sensing and their applications, and a strong interest in vision for intelligent systems and intelligent-system-based vision.

Dr. Gao was the recipient of the prestigious "National Plan for Young Talents" Award and the Hubei Province Funds for Distinguished Young Scientists. In addition, he is also a "Chutian Scholar" Distinguished Professor in Hubei. He serves as an Associate Editor for *Unmanned Systems*.